



In situ poly(methyl methacrylate)-templating generation and excellent catalytic performance of $\text{MnO}_x/\text{3DOM LaMnO}_3$ for the combustion of toluene and methanol

Yuxi Liu^a, Hongxing Dai^{a,*}, Jiguang Deng^{a,**}, Yucheng Du^{b,***}, Xinwei Li^a, Zhenxuan Zhao^a, Yuan Wang^a, Baozu Gao^a, Huanggen Yang^a, Guangsheng Guo^a

^a Laboratory of Catalysis Chemistry and Nanoscience, Department of Chemistry and Chemical Engineering, College of Environmental and Energy Engineering, Beijing University of Technology, Beijing 100124, PR China

^b Key Lab of Advanced Functional Materials, Ministry of Education, College of Materials Science and Engineering, Beijing University of Technology, Beijing 100124, PR China

ARTICLE INFO

Article history:

Received 18 January 2013

Received in revised form 26 March 2013

Accepted 23 April 2013

Available online 4 May 2013

Keywords:

Three-dimensionally ordered macroporous

perovskite

Supported manganese oxide catalyst

Metal oxide–support interaction

Toluene combustion

Methanol combustion

ABSTRACT

Rhombohedrally crystallized three-dimensionally ordered macroporous (3DOM) LaMnO_3 supported MnO_x (5, 8, 12, 16 wt% $\text{MnO}_x/\text{3DOM LaMnO}_3$) catalysts were prepared using the in situ tryptophan-assisted poly(methyl methacrylate)-templating strategy. Physicochemical properties of the materials were characterized by means of numerous analytical techniques, and their catalytic activities were evaluated for the combustion of toluene and methanol. It is shown that the $\text{MnO}_x/\text{3DOM LaMnO}_3$ samples displayed a 3DOM architecture and a high surface area of 19–31 m^2/g . The 12 wt% $\text{MnO}_x/\text{3DOM LaMnO}_3$ sample showed the highest oxygen adspecies concentration and the best low-temperature reducibility as well as the highly dispersed MnO_x particles on the LaMnO_3 surface, giving the highest TOF values of $7.9 \times 10^{-6} \text{ s}^{-1}$ for toluene combustion at 160 °C and $7.3 \times 10^{-6} \text{ s}^{-1}$ for methanol combustion at 80 °C. The apparent activation energies of the $\text{MnO}_x/\text{3DOM LaMnO}_3$ catalysts were 61–62 and 48–54 kJ/mol for toluene and methanol combustion, respectively. It is concluded that the excellent catalytic performance of 12 wt% $\text{MnO}_x/\text{3DOM LaMnO}_3$ was associated with its highest oxygen adspecies concentration, best low-temperature reducibility, and strong interaction between MnO_x and 3DOM LaMnO_3 .

© 2013 Elsevier B.V. All rights reserved.

1. Introduction

Most of volatile organic compounds (VOCs) are harmful to the atmosphere and human health. They can be removed via catalytic combustion. In the past years, supported noble metals, single or mixed transition metal oxides, and perovskite-type oxides (ABO_3) have been utilized for the combustion of VOCs. In spite of high performance at low temperatures, the applications of noble metal (e.g., Pt, Pd, and Rh)-based catalysts are limited due to their high cost, low thermal stability, easy sintering, and tendency to poisoning. As a potential alternative of noble metals, ABO_3 has received considerable attention in the catalytic oxidation of VOCs because they are low in cost and high in thermal stability [1].

The ABO_3 materials prepared by different methods, however, are usually nonporous and relatively low in surface area

(< 10 m^2/g), making the accessibility of reactant molecules to the active sites unfavorable. In this view, one solution of increasing the contact surface is to disperse ABO_3 on a support with a large surface area and thermal stability. For example, compared to the $\text{La}_{0.8}\text{Sr}_{0.2}\text{CoO}_3$, LaFeO_3 , and LaCoO_3 catalysts, the $\text{La}_{0.8}\text{Sr}_{0.2}\text{CoO}_3/\text{ZrO}_2$ [2], $\text{LaFeO}_3/\text{ZrO}_2$ [3], and $\text{LaCoO}_3/\text{CeO}_2$ [4] catalysts showed much better catalytic performance. The other solution is to load transition-metal oxides (MO_x) on ABO_3 . For instance, the $\text{Fe}_2\text{O}_3/\text{La}_{0.6}\text{Sr}_{0.4}\text{Co}_{0.8}\text{Fe}_{0.2}\text{O}_3$ [5], $\text{NiO}/\text{LaMnO}_3$ [6], and $\text{Co}_3\text{O}_4/\text{LaFe}_{0.7}\text{Cu}_{0.3}\text{O}_3$ [7] catalysts outperformed their transition-metal oxide counterparts.

For supported metal oxide catalysts, a particular interest is the strong metal–support interaction. There are synergetic effects between the metal oxide and the support, which can strongly influence electronic structures of the metal oxide catalysts [8]. A number of attempts have been made to identify the synergistic action between the metal oxide and the support, which has frequently been proposed to explain the high activities of $\text{Co}_3\text{O}_4/\text{ZrO}_2$ [9], $\text{Co}_3\text{O}_4\text{–MnO}_x/\text{Ce}_{0.85}\text{Zr}_{0.15}\text{O}_2$ [10], $\text{CuO}/\text{Ce}_{1-x}\text{Cu}_x\text{O}_{2-\delta}$ [11] for the oxidation of CO and VOCs.

It has been established that the size and dispersion of a metal oxide on support are crucial factors influencing its catalytic

* Corresponding author. Tel.: +86 10 6739 6118; fax: +86 10 6739 1983.

** Corresponding author. Tel.: +86 10 6739 6588; fax: +86 10 6739 6588.

***Corresponding author. Tel.: +86 10 6739 6129; fax: +86 10 6739 6129.

E-mail addresses: hxdai@bjut.edu.cn (H. Dai), jgdeng@bjut.edu.cn (J. Deng), ychengdu@bjut.edu.cn (Y. Du).

performance. According to the literature, however, most of the supported metal oxide (MO_x) catalysts prepared so far display bigger particle sizes (hundreds of nanometers) of MO_x and poor MO_x dispersion. Furthermore, the supported MO_x catalysts are usually prepared using the incipient wetness impregnation method, causing the difficulty in controlling the morphologies of the metal oxide. Therefore, it is highly desired to develop a facile and one-step approach for the synthesis of supported MO_x catalysts.

The poly(methyl methacrylate) (PMMA)-templating strategy is an effective route to obtain three-dimensionally ordered macroporous (3DOM) ABO_3 with relatively large surface areas [12]. Some chelating agents (citric acid, L-lysine, and ascorbic acid) or surfactants (ethylene glycol (EG), polyethylene glycol (PEG), and Pluronic P123) can be used to generate mesopores in the skeletons of macropores. The introduction of a suitable chelating agent or surfactant during the preparation process is beneficial for the improvement in catalytic performance. We envision that the catalytic activity would be enhanced if a certain amount of MO_x were loaded on the ABO_3 surface.

Recently, we have used the in situ PMMA-templating strategy to generate a series of $\text{MO}_x/3\text{DOM ABO}_3$ ($\text{M}=\text{Co}, \text{Mn}, \text{Cr}$; $\text{A}=\text{La}, \text{La}_{0.6}\text{Sr}_{0.4}$; $\text{B}=\text{Co}, \text{Mn}, \text{Cr}$) materials and observed that they showed excellent catalytic activities for the oxidation of typical VOCs. In this work, we report the novel in situ tryptophan-assisted PMMA-templating preparation, characterization, and catalytic performance of $\text{MnO}_x/3\text{DOM LaMnO}_3$ materials for the combustion of toluene and methanol.

2. Experimental

2.1. Catalyst preparation

The well-arrayed hard template PMMA microspheres with an average diameter of ca. 300 nm were synthesized according to the procedures described elsewhere [13].

The y wt% $\text{MnO}_x/3\text{DOM LaMnO}_3$ (y is the weight percent of Mn_2O_3 , $y=0, 5, 8, 12$, and 16) catalysts were prepared using the in situ tryptophan-assisted PMMA-templating strategy. In a typical fabrication, the desired amounts of $\text{La}(\text{NO}_3)_3 \cdot 6\text{H}_2\text{O}$ and $\text{Mn}(\text{NO}_3)_2$ (50 wt% aqueous solution) were dissolved in 3 mL of PEG (MW = 400 g/mol) and 3 mL of methanol (MeOH) at room temperature (RT) under stirring for 4 h to obtain a transparent solution. 1.0 g of L-tryptophan was dissolved in a nitric acid aqueous solution (5 mol/L). Then, the tryptophan-containing solution was mixed with the metal nitrate-containing transparent solution under stirring for 1 h to obtain a uniform precursor solution, to which a certain amount of MeOH was added to achieve a total metal concentration of 2.5 mol/L. Circa 2.0 g of the PMMA hard template was soaked in the above precursor solution for 4 h. After being filtered, the obtained wet PMMA template was dried in air at RT for 48 h, and then transferred to a ceramic boat which was placed in a tubular furnace. The thermal treatment process was divided into two steps: (i) the solid was first calcined in a N_2 flow of 200 mL/min at a ramp of $1^\circ\text{C}/\text{min}$ from RT to 300°C and kept at this temperature for 3 h, and then cooled to 50°C in the same atmosphere; and (ii) after being purged in an air flow of 100 mL/min, the solid was heated at a ramp of $1^\circ\text{C}/\text{min}$ from RT to 750°C and maintained at this temperature for 4 h.

For comparison purposes, we also prepared bulk LaMnO_3 (Bulk- LaMnO_3) and 12 wt% $\text{MnO}_x/\text{Bulk-LaMnO}_3$ samples. The Bulk- LaMnO_3 sample was prepared using the citric acid-complexing method described elsewhere [14]. The 12 wt% $\text{MnO}_x/\text{Bulk-LaMnO}_3$ sample was obtained via the incipient wetness impregnation route. The desired amount of $\text{Mn}(\text{NO}_3)_2 \cdot 6\text{H}_2\text{O}$ was dissolved in 1 mL of deionized water. 0.2 g of Bulk- LaMnO_3 was impregnated with the

Mn-containing solution for 4 h and then dried at 110°C in an oven for 12 h. The as-received solid was calcined in a muffle furnace from RT to 750°C and kept at this temperature for 4 h.

2.2. Catalyst characterization

X-ray diffraction (XRD) patterns of the samples were recorded on a Bruker D8 Advance diffractometer with $\text{Cu K}\alpha$ radiation and nickel filter ($\lambda=0.15406\text{ nm}$). Thermogravimetric analysis (TGA) and differential scanning calorimetric (DSC) analysis of the typical uncalcined samples were conducted (from RT to 700°C) in an air flow of 50 mL/min at a heating rate of $10^\circ\text{C}/\text{min}$ over a SDT Q600 (TA) apparatus. The scanning electron microscopic (SEM) images and energy-dispersive spectra (EDS) of the samples were recorded on a Gemini Zeiss Supra 55 apparatus (operating at 10 kV). Transmission electron microscopic (TEM) images as well as the selected-area electron diffraction (SAED) patterns of the samples were obtained using the JEOL-2010 equipment (operating at 200 kV). BET (Brunauer–Emmett–Teller) surface areas of the samples were measured via N_2 adsorption at -196°C on a Micromeritics ASAP 2020 analyzer with the samples outgassed at 300°C for 2.5 h under vacuum before measurement. X-ray photoelectron spectroscopy (XPS, VG CLAM 4 MCD analyzer) was used to determine the La 3d, Mn 2p, O 1s, and C 1s binding energies (BEs) of surface species using $\text{Mg K}\alpha$ ($h\nu=1253.6\text{ eV}$) as the excitation source. In order to remove the adsorbed water and carbonate species on the surface, the samples were pre-treated in O_2 (flow rate = 20 mL/min) at 600°C for 1 h and then cooled to RT, followed by transferring the pre-treated samples into the spectrometer in a transparent Glove Bag (Instruments for Research and Industry, USA) filled with helium. The pre-treated samples were outgassed in the preparation chamber (10^{-5} Torr) for 0.5 h and then introduced into the analysis chamber (3×10^{-9} Torr) for XPS spectrum recording. The C 1s signal at 284.6 eV was taken as a reference for BE calibration.

Hydrogen temperature-programmed reduction (H_2 -TPR) experiments were carried out on a chemical adsorption analyzer (Autochem II 2920, Micromeritics). Before TPR measurement, ca. 0.025 g of catalyst (40–60 mesh) was loaded to a quartz fixed-bed U-shaped micro-reactor (i.d. = 4 mm) and pre-treated in an O_2 flow of 30 mL/min at 500°C for 1 h. After being cooled in the same atmosphere to RT, the pre-treated sample was exposed to a flow (50 mL/min) of 5% H_2 –95% Ar (v/v) mixture and heated from RT to 850°C at a ramp of $10^\circ\text{C}/\text{min}$. The alteration in H_2 concentration of the effluent was monitored on-line by the chemical adsorption analyzer. The reduction band was calibrated against that of the complete reduction of a known standard of powdered CuO (Aldrich, 99.995%).

2.3. Catalytic evaluation

A continuous flow fixed-bed quartz micro-reactor (i.d. = 4 mm) was used to measure the catalytic activities of the samples at atmospheric pressure for the combustion of toluene and methanol. To minimize the effect of hot spots, 0.1 g of the catalyst sample (40–60 mesh) was diluted with 1.0 g of quartz sands (40–60 mesh). The total flow rate of the reactant mixture (1000 ppm VOC + O_2 + N_2 (balance)) was 33.3 mL/min, giving a toluene/ O_2 molar ratio of 1/400 and a SV of 20,000 mL/(g h). The 1000-ppm VOC was generated by passing a N_2 flow through a bottle containing pure toluene or methanol (A.R. grade) chilled in an ice-water isothermal bath. For the change of SV, we altered the total mass flow of feed gas mixture. Reactants and products were analyzed on-line by a gas chromatograph (GC-2010, Shimadzu) equipped with a flame ionization detector (FID) and a thermal conductivity detector (TCD), using a stabilwax@-DA column (30 m in length) for VOCs separation

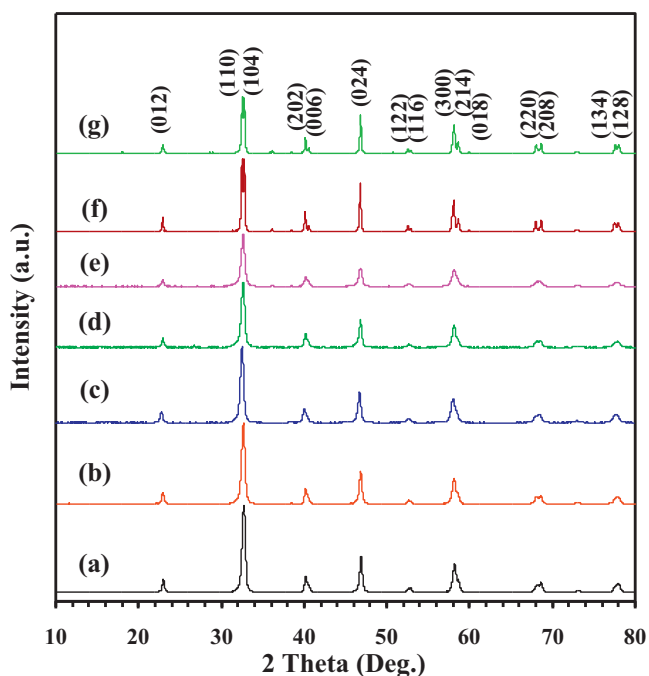


Fig. 1. XRD patterns of (a) 3DOM LaMnO₃, (b) 5 wt% MnO_x/3DOM LaMnO₃, (c) 8 wt% MnO_x/3DOM LaMnO₃, (d) 12 wt% MnO_x/3DOM LaMnO₃, (e) 16 wt% MnO_x/3DOM LaMnO₃, (f) Bulk-LaMnO₃, and (g) 12 wt% MnO_x/Bulk-LaMnO₃.

and a 1/8 in Carboxen 1000 column (3 m in length) for permanent gas separation. The balance of carbon throughout the investigation was estimated to be 99.5%.

3. Results and discussion

3.1. Crystal phase structure

Fig. 1 shows the XRD patterns of the as-prepared LaMnO₃ and *y* wt% MnO_x/LaMnO₃ samples. By comparing the XRD pattern of the standard LaMnO₃ sample (JCPDS PDF# 82-1152), one can realize that the XRD peaks of each sample in the 2θ range of 10–80° could be well indexed to be rhombohedral perovskite, as indicated in Fig. 1g. In other words, all of the samples were single-phase and of a rhombohedral crystal structure. Manganese nitrate would be decomposed into Mn₂O₃ after thermal treatment in air at 750 °C [15], but no signals due to the Mn₂O₃ phase were detected in the XRD patterns. The absence of simple metal oxides (such as La₂O₃, Mn₂O₃ or Mn₃O₄) in these samples indicates that the manganese oxide was highly dispersed on the surface of 3DOM LaMnO₃. The TGA/DSC profiles of the uncalcined 3DOM LaMnO₃ and 16 wt% MnO_x/LaMnO₃ samples (Fig. S1 of supplementary material) suggest that the calcination temperature of 750 °C was appropriate in the generation of single-phase perovskite LaMnO₃.

As can be seen from Table 1, the crystallite size (118 nm) estimated according to the Scherrer equation of the Bulk-LaMnO₃ sample was much bigger than that (41 nm) of 3DOM LaMnO₃ and those (26–35 nm) of the *y* wt% MnO_x/3DOM LaMnO₃ samples. The MnO_x nanoentities might act as a diffusion barrier and inhibited the crystal growth of the LaMnO₃ nanocrystallites. Similar results have been reported by other researchers [16].

3.2. Morphology, pore structure, and surface area

Figs. 2 and 3 show the representative SEM and TEM images as well as the SAED patterns of the LaMnO₃ and *y* wt% MnO_x/LaMnO₃ samples, respectively. It is observed that after calcination at 750 °C,

all of the 3DOM samples (except for the 16 wt% MnO_x/LaMnO₃ sample) displayed a high-quality 3DOM structure (Fig. 2a–h). The macropore sizes and wall thicknesses of these samples were 50–120 and 20–40 nm, respectively. With the loading of MnO_x to 12 wt%, there were the MnO_x nanoparticles highly dispersed on the surface of the 3DOM-structured LaMnO₃ samples (Fig. 2g and h). However, significant destruction of 3DOM structure (Fig. 2i and j) was observed in the 16 wt% MnO_x/LaMnO₃ sample, a result due to the high MnO_x loading. The real element compositions of the as-obtained samples were roughly in agreement with their corresponding normal compositions (Fig. S2 of the supplementary material).

Fig. 3 shows the representative TEM and high-resolution TEM (HRTEM) images of the LaMnO₃ and *y* wt% MnO_x/LaMnO₃ samples. The generation of LaMnO₃ perovskite phase was confirmed by its *d*-spacing (d_{LaMnO_3} (1 1 0) = 0.28 nm), which was close to the *d* value (d_{LaMnO_3} (1 1 0) = 0.2764 nm, JCPDS PDF# 82-1152) of single-phase LaMnO₃ (Fig. 3b, d, g, and i). At lower loadings (*y* = 5–8), it is hard to distinguish the morphology of the MnO_x and the LaMnO₃. However, several spherical Mn₂O₃ nanoparticles in the size range of 4–18 nm were observed on the surface of the 12 wt% MnO_x/LaMnO₃ sample (Fig. 3h and i), which was substantiated by the measurement of the *d*-spacing of the Mn₂O₃ nanoparticles ($d_{\text{Mn}_2\text{O}_3}$ (2 2 2) = 0.27 nm and $d_{\text{Mn}_2\text{O}_3}$ (4 4 0) = 0.17 nm), which was not far away from those (0.272 and 0.166 nm, respectively) of the standard Mn₂O₃ sample (JCPDS PDF# 41-1442). The recording of multiple bright electron diffraction rings in the SAED patterns (insets of Fig. 3b, d, g, j, and l) demonstrates that the LaMnO₃ and *y* wt% MnO_x/LaMnO₃ samples were polycrystalline.

N₂ adsorption–desorption isotherms and pore-size distributions of the 3DOM LaMnO₃ and *y* wt% MnO_x/LaMnO₃ samples are shown in Fig. 4 and their pore parameters and BET surface areas are summarized in Table 1. It is seen from Fig. 4A that all of the samples displayed a similar type II isotherm with H3 (p/p_0 = 0.9–1.0) and H2 (p/p_0 = 0.7–0.9) hysteresis loops, indicating that these samples were materials with macroporous and mesoporous structures. There was a difference in size of H3 or H2 hysteresis loop between 3DOM LaMnO₃ and *y* wt% MnO_x/LaMnO₃, demonstrating that the 3DOM structure was modified by the loaded manganese oxide, which also played a role in influencing the pore-size distributions and BET surface areas of *y* wt% MnO_x/LaMnO₃. There was a pore-size distribution scattering from 4 to 80 nm in each of the samples (Fig. 4B). As can be seen from Table 1, the BET surface area of the 3DOM LaMnO₃ sample was 31.4 m²/g. With the loading of MnO_x from 5 to 16 wt%, the BET surface area decreased from 31.0 to 19.1 m²/g. The Bulk-LaMnO₃ and 12 wt% MnO_x/Bulk-LaMnO₃ samples possessed a surface area of 7.0–7.3 m²/g. The *y* wt% MnO_x/3DOM LaMnO₃ samples exhibited a pore volume of 0.060–0.085 cm³/g.

Amino acid is usually considered as a capping agent or crystal growth modifier [17,18]. The interaction between amino acid and metal precursors has been well documented in the literature [19]. During the preparation process of 3DOM LaMnO₃ with L-tryptophan as chelating agent, La and Mn ions could interact with the amine and carboxylate functional groups to form the metal–tryptophan complexes. These metal–tryptophan complexes might play a critical role in the generation of mesoporous skeletons after the subsequent thermal treatments in various environments.

3.3. Surface composition, Mn oxidation state, and oxygen species

XPS is an effective technique to gain the information related to surface element compositions, metal oxidation states, and adsorbed species of a solid material. Fig. 5 illustrates the Mn 2p_{3/2} and O 1s XPS spectra of the LaMnO₃ and *y* wt% MnO_x/LaMnO₃ samples, and their quantitative analysis results are summarized in Table 2. From Table 2, one can find that the surface La/Mn

Table 1Preparation conditions, crystallite sizes, BET surface areas, average pore sizes, and pore volumes of the LaMnO_3 and y wt% $\text{MnO}_x/\text{LaMnO}_3$ samples.

Catalyst	Method	Hard template/surfactant	Calcination condition	Crystallite size ^a (nm)	BET surface area (m^2/g)	Pore volume (cm^3/g)	Average pore size (nm) ^b
Bulk- LaMnO_3	Citric acid-complexing	—/—	850 °C 4 h (in air)	118	7.3	—	—
3DOM LaMnO_3	PMMA-templating	PMMA/(L-tryptophan + PEG400)	300 °C 3 h (in N_2) → 750 °C 4 h (in air)	41	31.4	0.085	120
5 wt% $\text{MnO}_x/3\text{DOM LaMnO}_3$	In situ PMMA-templating	PMMA/(L-tryptophan + PEG400)	300 °C 3 h (in N_2) → 750 °C 4 h (in air)	35	31.0	0.080	110
8 wt% $\text{MnO}_x/3\text{DOM LaMnO}_3$	In situ PMMA-templating	PMMA/(L-tryptophan + PEG400)	300 °C 3 h (in N_2) → 750 °C 4 h (in air)	31	28.1	0.082	110
12 wt% $\text{MnO}_x/3\text{DOM LaMnO}_3$	In situ PMMA-templating	PMMA/(L-tryptophan + PEG400)	300 °C 3 h (in N_2) → 750 °C 4 h (in air)	28	25.0	0.075	100
16 wt% $\text{MnO}_x/3\text{DOM LaMnO}_3$	In situ PMMA-templating	PMMA/(L-tryptophan + PEG400)	300 °C 3 h (in N_2) → 750 °C 4 h (in air)	26	19.1	0.060	50
12 wt% $\text{MnO}_x/\text{Bulk-LaMnO}_3$	Impregnation	—/—	750 °C 4 h (in air)	111	7.0	—	—

^a Data calculated according to the full width at half-maximum of the (1 1 0) line and the Scherrer equation.^b Estimated according to the SEM and TEM images.

molar ratio (1.15) of the 3DOM LaMnO_3 sample was higher than its nominal La/Mn molar ratio (1.00), suggesting the presence of La enrichment on the surface of 3DOM LaMnO_3 [20]. The surface La/Mn molar ratios of x wt% $\text{MnO}_x/3\text{DOM LaMnO}_3$ were in the range of 0.71–0.90, indicative of the occurrence of Mn enrichment on the surface of these samples. It can be observed from Fig. 5A that the asymmetrical Mn $2p_{3/2}$ XPS spectrum of each sample could be decomposed to three components at BE = 641.2, 642.7, and

644.7 eV, assignable to the surface Mn^{3+} and Mn^{4+} species and the satellite of Mn^{3+} species [20], respectively. The discrepancy in surface $\text{Mn}^{4+}/\text{Mn}^{3+}$ molar ratio of these samples was a result due to the different preparation approaches. The surface $\text{Mn}^{4+}/\text{Mn}^{3+}$ molar ratio (1.1) of the 3DOM LaMnO_3 sample was higher than that (0.8) of the bulk counterpart. Among the y wt% $\text{MnO}_x/\text{LaMnO}_3$ samples, with the loading of MnO_x , the 12 wt% $\text{MnO}_x/3\text{DOM LaMnO}_3$ sample exhibited the highest surface $\text{Mn}^{4+}/\text{Mn}^{3+}$ molar ratio (1.3). A further

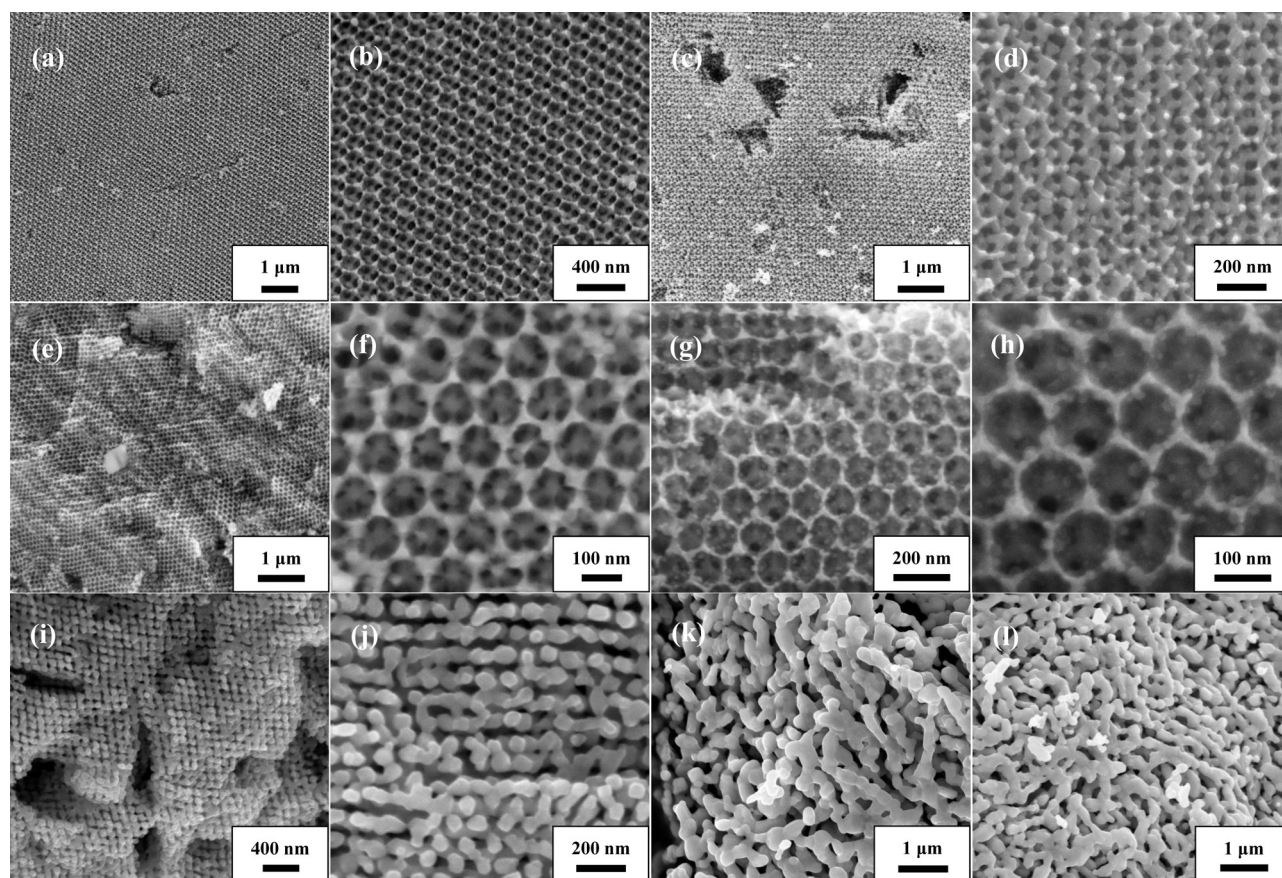


Fig. 2. SEM images of (a and b) 3DOM LaMnO_3 , (c and d) 5 wt% $\text{MnO}_x/3\text{DOM LaMnO}_3$, (e and f) 8 wt% $\text{MnO}_x/3\text{DOM LaMnO}_3$, (g and h) 12 wt% $\text{MnO}_x/3\text{DOM LaMnO}_3$, (i and j) 16 wt% $\text{MnO}_x/3\text{DOM LaMnO}_3$, (k) 12 wt% $\text{MnO}_x/\text{Bulk-LaMnO}_3$, and (l) Bulk- LaMnO_3 .

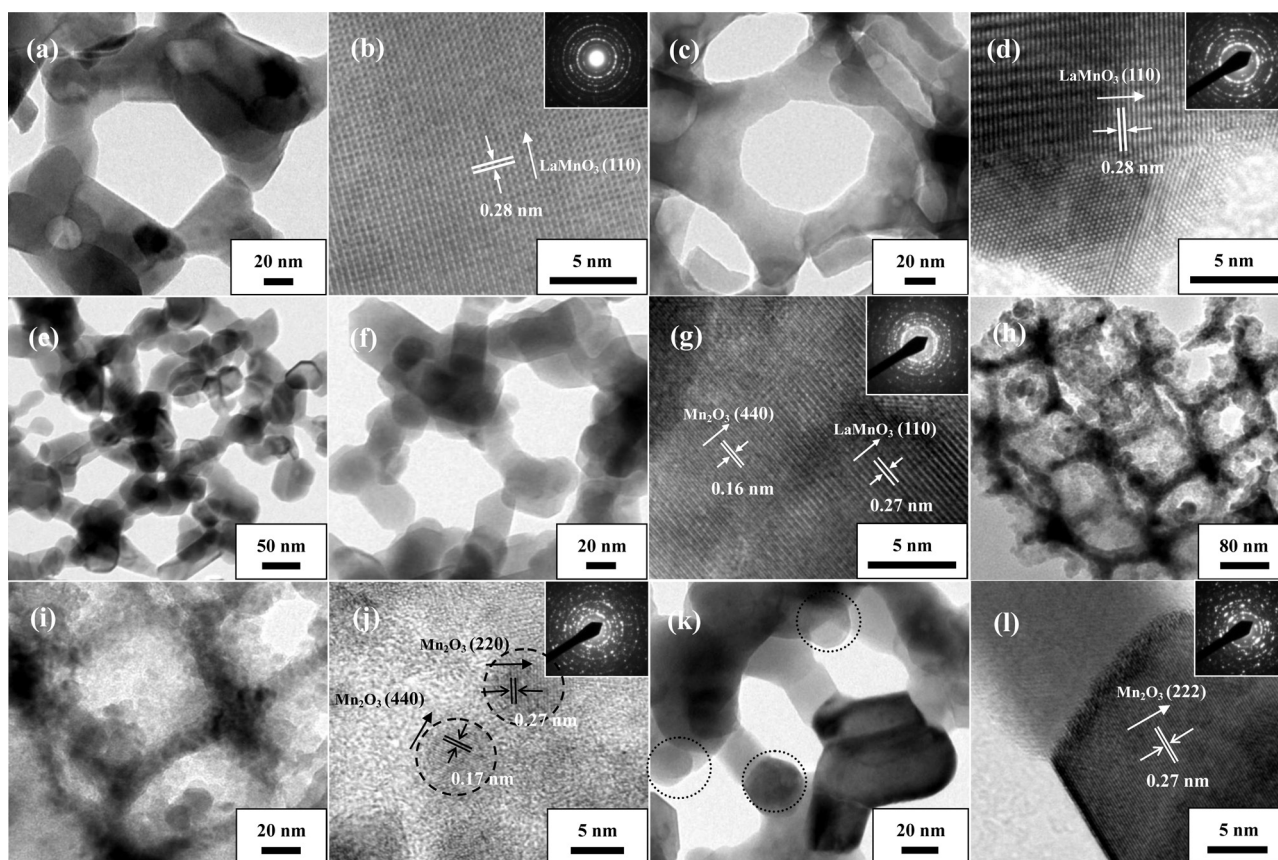


Fig. 3. TEM and high-resolution TEM images as well as the SAED patterns (insets) of (a and b) 3DOM LaMnO₃, (c and d) 5 wt% MnO_x/3DOM LaMnO₃, (e–g) 8 wt% MnO_x/3DOM LaMnO₃, (h–j) 12 wt% MnO_x/3DOM LaMnO₃, and (k and l) 16 wt% MnO_x/3DOM LaMnO₃.

rise in MnO_x loading, however, led to a drop in surface Mn⁴⁺/Mn³⁺ atomic ratio (0.8). The discrepancy in surface Mn⁴⁺/Mn³⁺ molar ratio reflected the difference in MnO_x dispersion on the surface of LaMnO₃. With lower MnO_x loading (5–12 wt%), manganese species

in the form of Mn⁴⁺–O_{ads} Lewis acid–base pairs [21] was well dispersed on the LaMnO₃ surface; at a higher MnO_x loading (16 wt%), however, there was the formation of bigger MnO_x particles on the surface of LaMnO₃ and a phase separation of MnO_x and LaMnO₃

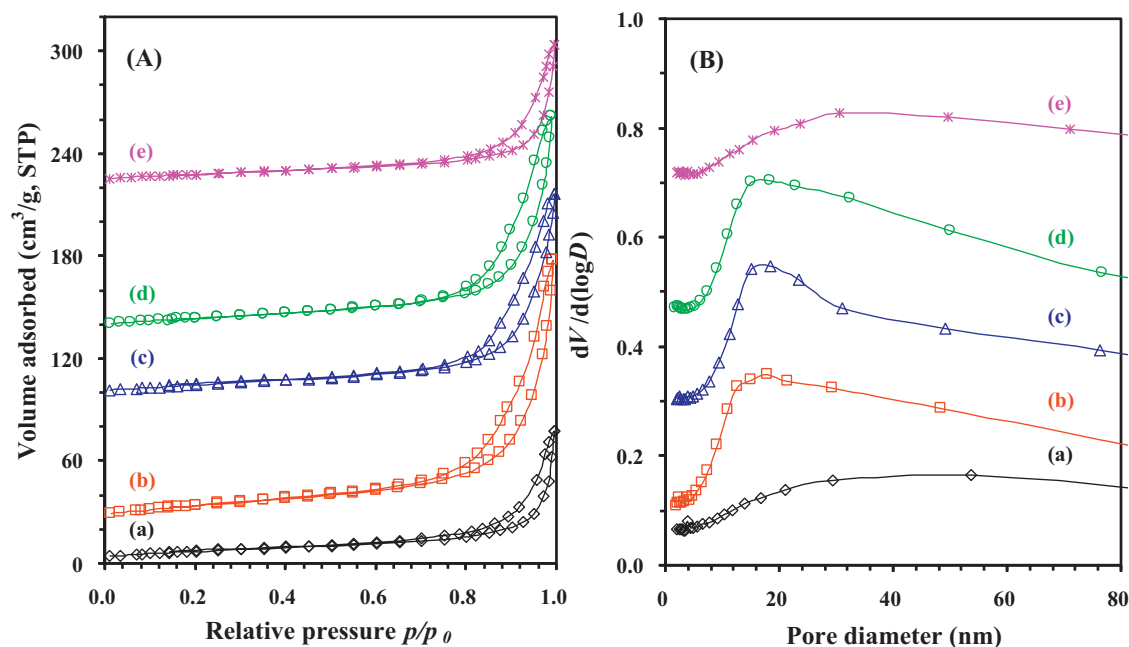


Fig. 4. (A) Nitrogen adsorption–desorption isotherms and (B) pore-size distributions of (a) 3DOM LaMnO₃, (b) 5 wt% MnO_x/3DOM LaMnO₃, (c) 8 wt% MnO_x/3DOM LaMnO₃, (d) 12 wt% MnO_x/3DOM LaMnO₃, and (e) 16 wt% MnO_x/3DOM LaMnO₃.

Table 2
Surface element compositions, H₂ consumptions, and catalytic activities of the LaMnO₃ and y wt% MnO_x/LaMnO₃ samples.

Catalyst	La/Mn molar ratio	O _{ads} /O _{latt} molar ratio	Mn ⁴⁺ /Mn ³⁺ molar ratio	H ₂ consumption ^a (mmol/g)					Toluene combustion activity ^b				Methanol combustion activity ^b	
				<500 °C				>500 °C	T _{10%} (°C)	T _{50%} (°C)	T _{90%} (°C)	T _{10%} (°C)	T _{50%} (°C)	T _{90%} (°C)
				α	β	γ	total							
Bulk-LaMnO ₃	1.01	0.87	0.8	–	–	–	0.97	2.17	212	263	300	141	179	202
3DOM LaMnO ₃	1.15	1.31	1.1	0.12	0.80	0.55	1.47	1.88	170	210	228	101	142	158
5 wt% MnO _x /3DOM LaMnO ₃	0.89	1.39	1.1	0.26	0.89	0.76	1.91	1.77	164	208	225	98	137	155
8 wt% MnO _x /3DOM LaMnO ₃	0.83	1.60	1.2	0.32	1.51	0.90	2.77	1.31	160	203	222	88	130	151
12 wt% MnO _x /3DOM LaMnO ₃	0.75	1.93	1.3	0.58	1.65	1.17	3.40	0.92	152	193	215	76	121	137
16 wt% MnO _x /3DOM LaMnO ₃	0.71	1.42	0.8	0.44	1.69	1.25	3.38	1.00	160	201	222	85	132	154
12 wt% MnO _x /Bulk-LaMnO ₃	0.90	0.89	0.6	–	–	–	–	–	210	260	296	140	176	196

^a The data were obtained by quantitatively analyzing the H₂-TPR profiles.
^b The catalytic activities were measured under the conditions of toluene or methanol concentration = 1000 ppm, toluene or methanol/O₂ molar ratio = 1/400, and SV = 20,000 mL/(g h).

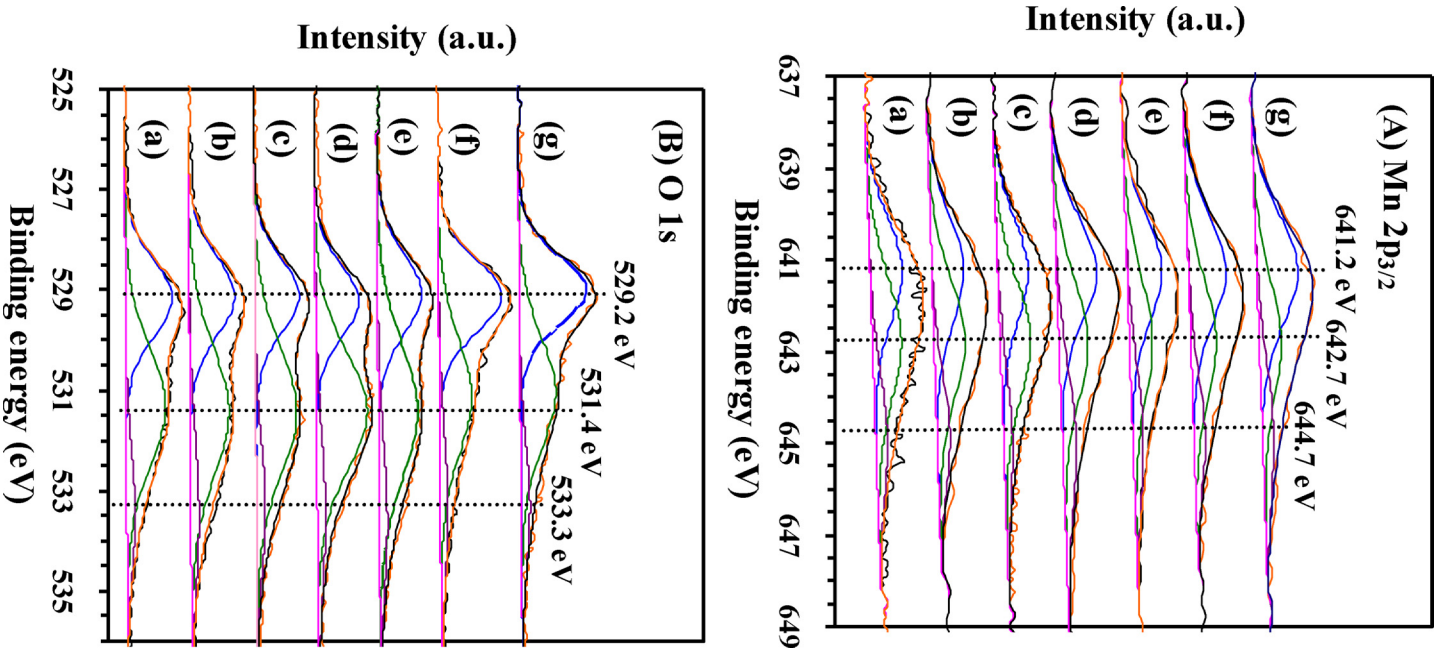


Fig. 5. (A) Mn 2p_{3/2} and (B) O 1s XPS spectra of (a) 3DOM LaMnO₃, (b) 5 wt% MnO_x/3DOM LaMnO₃, (c) 8 wt% MnO_x/3DOM LaMnO₃, (d) 12 wt% MnO_x/3DOM LaMnO₃, (e) 16 wt% MnO_x/3DOM LaMnO₃, (f) Bulk-LaMnO₃, and (g) 12 wt% MnO_x/Bulk-LaMnO₃.

would take place around the interfacial region of LaMnO₃. This deduction was substantiated by the HRTEM observations (Fig. 3). As shown in Fig. 5B, the asymmetrical O 1s spectrum of each sample could be decomposed to three components at BE = 529.2, 531.4, and 533.3 eV, attributable to the surface lattice oxygen (O_{latt}), adsorbed oxygen (O₂[–], O₂^{2–} or O[–]) and carbonate, and adsorbed molecular water [20] species, respectively. Due to the pre-treatment of the samples in an O₂ flow at 600 °C before XPS measurements, the amounts of surface OH[–] and CO₃^{2–} species

on the surface of the pre-treated samples would be minimized. Moreover, we could decompose each of the C 1s XPS spectra (Fig. S3 of the supplementary material) of the typical samples to three components at BE = 284.6 and 286.4 eV (due to surface contamination carbon) and 288.4 eV (due to surface carbonate species) [22]. The content of the surface carbonate species were low (Table S1 of the supplementary material) and almost retained unchanged on the surface of the Bulk-LaMnO₃, 3DOM LaMnO₃, and 12 wt% MnO_x/3DOM LaMnO₃ samples. Therefore, the O_{ads} species were mainly adsorbed oxygen species. In other words, the O_{ads}/O_{latt} molar ratios of the samples could reflect their O_{ads} species concentrations to some extent. The surface O_{ads}/O_{latt} molar ratio (1.31) of the 3DOM LaMnO₃ sample was much higher than that (0.87) of the bulk counterpart, indicating that the sample with a higher surface area possessed a more amount of electrophilic oxygen species, in good agreement with the observations in our previous studies [23]. The O_{ads}/O_{latt} molar ratio increased remarkably after the doping of MnO_x to the LaMnO₃ support, a result due to the presence of strong metal oxide–support interactions (SMSI). The increase in surface active oxygen species was beneficial for the enhancement in catalytic performance for deep oxidation reactions [24]. The SMSI is generally referred to the mutual electronic interaction between metal and oxide support. The SMSI was originally observed in the TiO₂-supported Pt catalyst, where the support exhibited variable valence [8]. Tan et al. also observed that Pd changed the oxidation state of Mn in the Pd/MnO_x catalyst and the tuning of electronic structure of Pd by MnO_x could properly be explained in terms of the SMSI [25]. In our present studies, the changes in surface Mn⁴⁺/Mn³⁺ and O_{ads}/O_{latt} molar ratios induced by the loading of MnO_x suggest the presence of the SMSI between MnO_x NPs and 3DOM LaMnO₃ support, which favored the enhancement in catalytic performance. When a metal oxide phase is deposited on the surface of a support, the SMSI can exist, and the binding energy of Mn 2p_{3/2} would be shifted a few tenths of eV toward higher binding energies [26]. In our present study, the Mn 2p_{3/2} signal of the 3DOM LaMnO₃ sample was centered at BE = ca. 641.9 eV, rather close to those of the LaMnO₃ samples reported in the literature [27,28]. After loading of MnO_x, however, the Mn 2p_{3/2} signals of the y wt% MnO_x/LaMnO₃ samples were shifted to higher BE values (ca. 642.2 eV). Kumar et al. [29] also observed a shift in BE value (ca. 0.5 eV) after loading of Ag on La_{0.8}Ba_{0.2}MnO₃. Working on the XPS investigations of Ag/MnO_x, Qu et al. [30] found that the supported Ag promoted the rise in Mn⁴⁺ concentration. Therefore, the loading of MnO_x resulted in a shift in the BE value of Mn 2p.

3.4. Reducibility

H₂-TPR is an ideal tool to examine the reducibility of a solid oxide catalyst. Fig. 6A illustrates the H₂-TPR profiles of the LaMnO₃ and y wt% MnO_x/LaMnO₃ samples. The reduction of each sample experienced two steps in the range of 50–500 and 500–900 °C. The reduction temperatures (348 and 830 °C) of the bulk LaMnO₃ sample were much higher than those (192, 284, 386, and 721 °C) of the 3DOM-structured counterpart, indicating that formation of a porous structure facilitated the reduction of the sample. For each porous sample, the first reduction peak can be decomposed into three (α , β , and γ) peaks. The α peak was due to the removal of a small amount of surface oxygen adspecies [31]; the β peak was attributed to the reduction of Mn⁴⁺ to Mn³⁺ and a single electron reduction of Mn³⁺ (located in a highly coordination-unsaturated microenvironment) to Mn²⁺ [31]; and the γ peak was the single-electron reduction of Mn³⁺ (located in a coordination-unsaturated microenvironment) to Mn²⁺ [31]. The second reduction (ϵ) peak above 500 °C was due to the reduction of the Mn³⁺ left in the bulk LaMnO₃ lattice to Mn²⁺ [31]. Quantitative analyses on these peaks can give the H₂

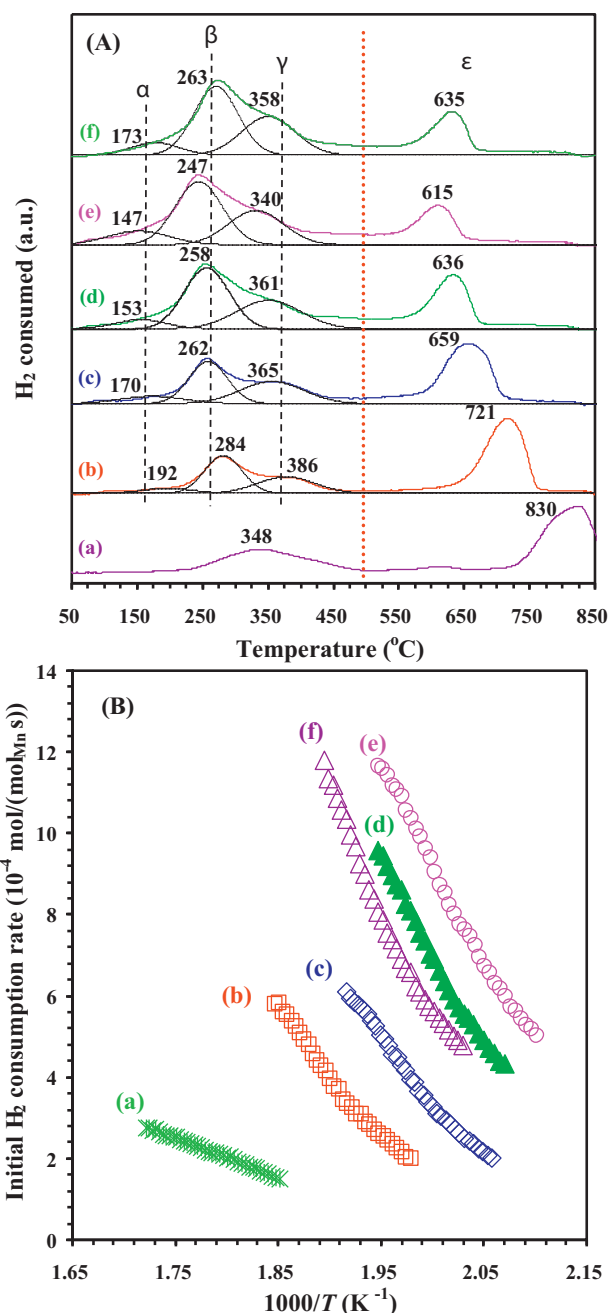


Fig. 6. (A) H₂-TPR profiles and (B) initial H₂ consumption rate as a function of inverse temperature of (a) Bulk-LaMnO₃, (b) 3DOM LaMnO₃, (c) 5 wt% MnO_x/3DOM LaMnO₃, (d) 8 wt% MnO_x/3DOM LaMnO₃, (e) 12 wt% MnO_x/3DOM LaMnO₃, and (f) 16 wt% MnO_x/3DOM LaMnO₃.

consumptions, as summarized in Table 2. It is observed that the H₂ consumptions corresponding to the amounts of surface oxygen adspecies were 0.26, 0.32, 0.58, and 0.44 mmol/g for the y wt% MnO_x/3DOM LaMnO₃ (y = 5, 8, 12 and 16) samples, respectively, whereas that was 0.12 mmol/g for the 3DOM LaMnO₃ sample. Previous studies provided strong evidence that the rise in surface active oxygen species concentration could lead to enhanced catalytic performance for the deep oxidation of VOCs [24]. In the past years, a number of researchers [20,31–33] pre-treated the Mn-based perovskite samples in an inert or oxygen flow in the range of 400–600 °C during the H₂-TPR process. It is supposed that 500 °C was high enough in temperature to remove most of the surface adsorbed hydroxide and hydrocarbonate species on the

surface of the samples. Therefore, the re-oxidation of the samples by water derived from the decomposition of surface hydrocarbonate or hydroxides during the TPR process would be minimized.

A large number of works have demonstrated that the amount (δ) of nonstoichiometric oxygen accommodated within the lattice of $\text{LaMnO}_{3+\delta}$ falls into the range of 0.12–0.16, which corresponds to a H_2 consumption of 0.49–0.66 mmol/g below 600 °C [34]. It means that all of the Mn^{4+} ions in $\text{LaMnO}_{3+\delta}$ have been reduced to Mn^{3+} . For our LaMnO_3 and y wt% $\text{MnO}_x/\text{LaMnO}_3$ samples, the H_2 consumption of the β peak was in the range 0.80–1.69 mmol/g, much higher than the above values. This result suggests that in addition to the reduction of Mn^{4+} to Mn^{3+} , there was possible partial reduction of Mn^{3+} located in a highly coordination-unsaturated microenvironment to Mn^{2+} on the surfaces of MnO_x and LaMnO_3 . That is to say, the partial reduction of the Mn^{3+} species in catalysts led to the rise in H_2 consumption at lower temperatures. From Table 2, one can see that the low-temperature (<500 °C) H_2 consumption increased in the order of Bulk- LaMnO_3 < 3DOM LaMnO_3 < 5 wt% $\text{MnO}_x/3\text{DOM LaMnO}_3$ < 8 wt% $\text{MnO}_x/3\text{DOM LaMnO}_3$ < 16 wt% $\text{MnO}_x/3\text{DOM LaMnO}_3$ < 12 wt% $\text{MnO}_x/3\text{DOM LaMnO}_3$.

It has been reported that with the rise in manganese nonstoichiometry in $\text{LaMnO}_{3+\delta}$, cation vacancy array was perturbed by oxygen vacancies which could trap Mn^{3+} ions, resulting in the easier reduction of Mn^{4+} [35]. But the excess doping of manganese oxide (e.g., 16 wt% $\text{MnO}_x/3\text{DOM LaMnO}_3$) might cause strong sintering of MnO_x nanoparticles, which would result in the shifting of the reduction peaks to higher temperatures. The changes in reduction temperature and H_2 consumption of the y wt% $\text{MnO}_x/3\text{DOM LaMnO}_3$ samples indicate that there was a strong interaction between MnO_x and 3DOM LaMnO_3 . The loading of MnO_x could also induce such changes. The loading of a metal oxide may lead to the weakening of the metal–oxygen bond strength in the parent oxide [36]. In a similar way, therefore, the loading of manganese oxide could also facilitate the reduction of the catalyst.

It has been generally accepted that the low-temperature reducibility of a catalyst can be conveniently evaluated by using the initial H_2 consumption rate [37]. The initial H_2 consumption rate was calculated according to the H_2 amount consumed per mol of Mn per second, which corresponded to the initial 25% area of the first reduction peak where no phase transformation of the catalyst occurred. Fig. 6B shows the initial H_2 consumption rate as a function of inverse temperature of the LaMnO_3 and y wt% $\text{MnO}_x/\text{LaMnO}_3$ samples. It is clearly seen that the initial H_2 consumption rates of the samples decreased in the order of 12 wt% $\text{MnO}_x/3\text{DOM LaMnO}_3$ > 8 wt% $\text{MnO}_x/3\text{DOM LaMnO}_3$ > 16 wt% $\text{MnO}_x/3\text{DOM LaMnO}_3$ > 5 wt% $\text{MnO}_x/3\text{DOM LaMnO}_3$ > 3DOM LaMnO_3 > Bulk- LaMnO_3 . Such trends in low-temperature reducibility were in good consistence with the sequence of catalytic performance shown below.

3.5. Catalytic performance

In the blank experiments (only quartz sands were loaded in the micro-reactor) under the conditions of toluene or methanol concentration = 1000 ppm, toluene or methanol/ O_2 molar ratio = 1/400, and SV = 20,000 mL/(g h), no significant toluene and methanol conversions were observed at 400 °C for toluene combustion and 200 °C for methanol combustion. These results indicate that no significant homogeneous reactions took place under the adopted reaction conditions. According to the Weisz–Prater criterion, when the effectiveness factor $\eta \geq 0.95$ and reaction order $n = 1$, the dimensionless Weisz–Prater parameter (N_{W-P}) value is less than 0.3, which can be considered a sufficient condition for the absence of significant pore diffusion limitations [38]. At toluene and methanol conversion $\leq 15\%$, we carried out the Weisz–Prater analysis (supplementary material) and calculated the N_{W-P} values, which were

in the range of 0.0088–0.011 and 0.012–0.014. Obviously, the N_{W-P} values obtained in our present investigation were much less than 0.3. Therefore, no significant mass transfer limitations existed in our catalytic system. The heat transfer issue can be checked by using the Koros–Nowak test (supplementary material) [39]. The calculated results (Table S2 of the supplementary material) indicate that the discrepancies in turnover frequency $\text{TOF}_{\text{MnO}_x}$ (calculated according to the reaction rates and molar amounts of MnO_x in y wt% $\text{MnO}_x/\text{LaMnO}_3$) value of the y wt% $\text{MnO}_x/3\text{DOM LaMnO}_3$ catalysts either for toluene combustion or for methanol combustion were low. Hence, no significant heat transfer problems were present in our study.

Fig. S4 (supplementary material) shows the catalytic activities of the LaMnO_3 and y wt% $\text{MnO}_x/\text{LaMnO}_3$ samples for the combustion of toluene and methanol at 20,000 mL/(g h). Obviously, toluene or methanol conversion increased with the rise in temperature, and the 12 wt% $\text{MnO}_x/\text{LaMnO}_3$ catalyst performed the best. Table 2 summarizes the catalytic activities of these samples. The reaction temperatures $T_{50\%}$ and $T_{90\%}$ (corresponding to VOC conversion = 50 and 90%) are used to evaluate the catalytic performance of the samples. Apparently, 3DOM LaMnO_3 performed much better than Bulk- LaMnO_3 . $T_{90\%}$ values of 228 °C for toluene combustion and 158 °C for methanol combustion were achieved over the 3DOM LaMnO_3 catalyst, whereas they were 300 °C for toluene combustion and 202 °C for methanol combustion over the Bulk- LaMnO_3 catalyst. Among the LaMnO_3 and y wt% $\text{MnO}_x/\text{LaMnO}_3$ catalysts, 12 wt% $\text{MnO}_x/\text{LaMnO}_3$ showed the best catalytic activity, giving the $T_{50\%}$ and $T_{90\%}$ values of 193 and 215 °C for toluene combustion and 121 and 137 °C for methanol combustion, respectively. As expected, toluene or methanol conversion increased with the drop in SV (Fig. S5 of the supplementary material), indicating that the extension in contact time was favorable for the conversion of toluene or methanol. It is worth pointing out that toluene and methanol were completely oxidized to CO_2 and H_2O over the as-prepared catalysts, no other incomplete oxidation products were detected in the catalytic system, which was also confirmed by the good carbon balance (ca. 99.5%) in each run.

It is better to use the VOC consumption rate for comparison in catalytic performance of the samples. Shown in Fig. 7A and B are toluene and methanol consumption rates ($\mu\text{mol}/(\text{g s})$) as a function of temperature over the LaMnO_3 and y wt% $\text{MnO}_x/\text{LaMnO}_3$ catalysts at 20,000 mL/(g h), respectively. Obviously, toluene or methanol consumption rate increased with the rise in temperature. Table 3 summarizes the catalytic reaction rates and TOF values of these samples. The reaction rates and TOF values at 160 °C for toluene combustion and at 80 °C for methanol combustion (corresponding to VOC conversion < 15%) are used to evaluate the performance of the catalysts. Apparently, toluene or methanol consumption rate over Bulk- LaMnO_3 was considerably lower than those over 3DOM LaMnO_3 and y wt% $\text{MnO}_x/3\text{DOM LaMnO}_3$. The consumption rate normalized per gram of catalyst was 0.014 $\mu\text{mol}/(\text{g s})$ for toluene combustion and 0.0094 $\mu\text{mol}/(\text{g s})$ for methanol combustion over the 3DOM LaMnO_3 catalyst, whereas it was 0.0013 $\mu\text{mol}/(\text{g s})$ for toluene combustion and 0.00092 $\mu\text{mol}/(\text{g s})$ for methanol combustion over the Bulk- LaMnO_3 catalyst. Among the LaMnO_3 and y wt% $\text{MnO}_x/\text{LaMnO}_3$ catalysts, the 12 wt% $\text{MnO}_x/\text{LaMnO}_3$ catalyst showed the highest VOC consumption rate (0.029 $\mu\text{mol}/(\text{g s})$ for toluene combustion and 0.027 $\mu\text{mol}/(\text{g s})$ for methanol combustion). At the same temperatures (when VOC conversion < 15%), VOC consumption rate decreased in the order of 12 wt% $\text{MnO}_x/\text{LaMnO}_3$ > 16 wt% $\text{MnO}_x/\text{LaMnO}_3$ \approx 8 wt% $\text{MnO}_x/\text{LaMnO}_3$ > 5 wt% $\text{MnO}_x/\text{LaMnO}_3$ > 3DOM LaMnO_3 > 12 wt% $\text{MnO}_x/\text{Bulk-LaMnO}_3$ > Bulk- LaMnO_3 , in good agreement with the sequences of surface oxygen species concentration and low-temperature reducibility of these materials. When toluene or methanol consumption rates ($\mu\text{mol}/(\text{m}^2 \text{ h})$) were normalized per

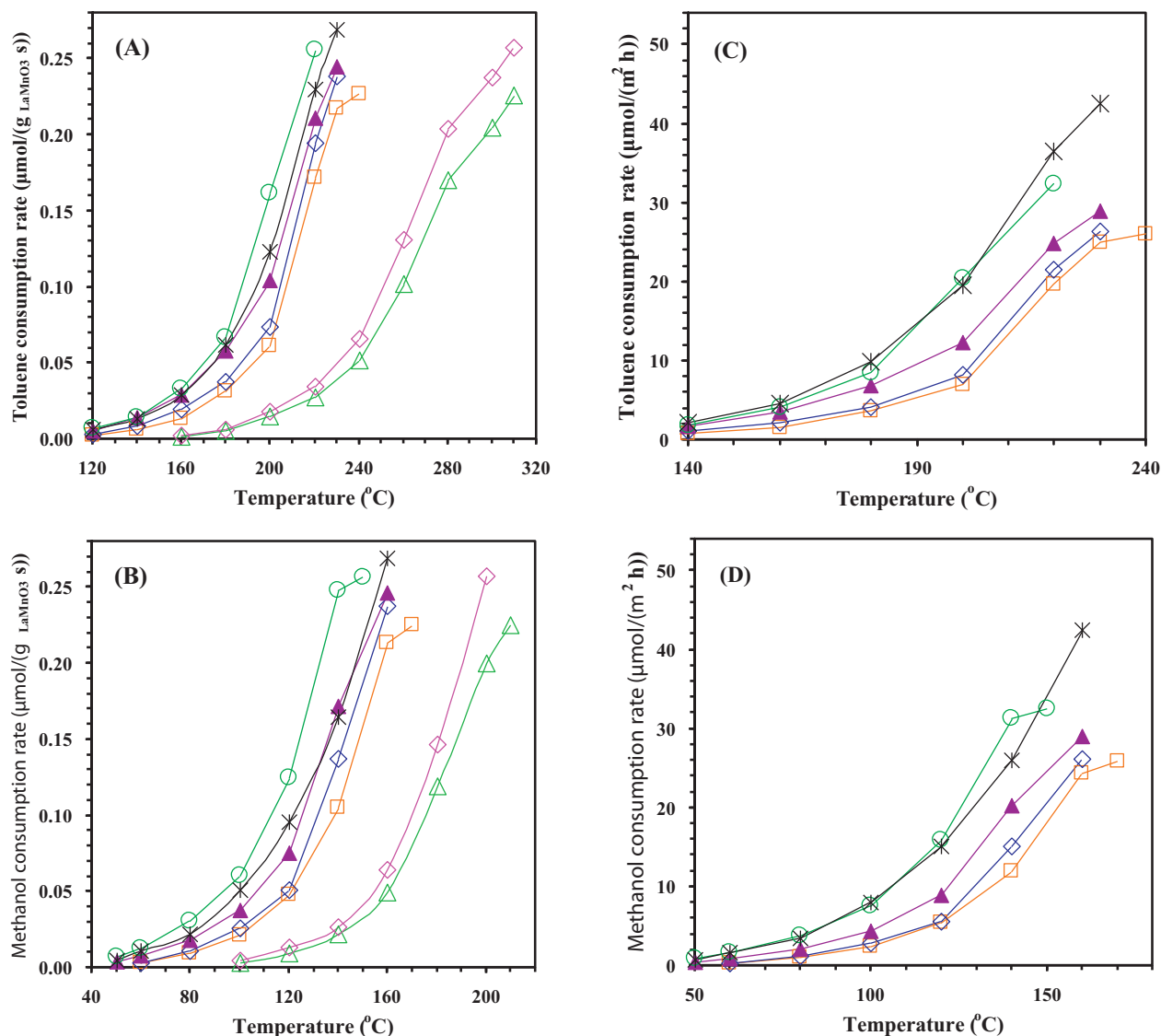


Fig. 7. (A and C) Toluene consumption rate and (B and D) methanol consumption rate as a function of reaction temperature over (□) 3DOM LaMnO₃, (◇) 5 wt% MnO_x/3DOM LaMnO₃, (▲) 8 wt% MnO_x/3DOM LaMnO₃, (○) 12 wt% MnO_x/3DOM LaMnO₃, (✱) 16 wt% MnO_x/3DOM LaMnO₃, (△) Bulk-LaMnO₃, (◆) 12 wt% MnO_x/Bulk-LaMnO₃.

surface area of catalyst (Fig. 7C and D), however, catalytic activities of the samples showed a change trend slightly different from that of toluene or methanol consumption rates normalized per gram of catalyst, and the 16 wt% MnO_x/LaMnO₃ sample gave the highest toluene consumption rate. This result was due to the lower surface area of 16 wt% MnO_x/LaMnO₃.

We suppose that the catalytic sites might be the Mn species in the LaMnO₃ and *y* wt% MnO_x/LaMnO₃ catalysts. The turnover frequencies (TOF_{Toluene} and TOF_{Methanol}) were calculated according to the reaction rates for toluene and methanol combustion and molar amounts of Mn in LaMnO₃ and *y* wt% MnO_x/LaMnO₃, respectively. Fig. 8 shows toluene and methanol consumption rates normalized per gram of LaMnO₃ and per surface area of catalyst and TOF_{Toluene} or TOF_{Methanol} as a function of MnO_x loading of the LaMnO₃ and *y* wt% MnO_x/LaMnO₃ samples at 160 °C for toluene combustion and 80 °C for methanol combustion. It is clearly seen that toluene or methanol consumption rate first increased with the rise in MnO_x loading up to 12 wt%, and then slightly decreased or maintained unchanged when MnO_x loading was 16 wt%. Over the 12 wt% MnO_x/3DOM LaMnO₃ catalyst, the TOF_{Toluene} and TOF_{Methanol} values were 7.9×10^{-6} and $7.3 \times 10^{-6} \text{ s}^{-1}$, respectively, much higher

than those ($3.3 \times 10^{-6} \text{ s}^{-1}$ and $2.3 \times 10^{-6} \text{ s}^{-1}$, respectively) over the 3DOM LaMnO₃ catalyst. This result indicates that a synergistic effect between the MnO_x and 3DOM LaMnO₃ was beneficial for enhancement in catalytic performance.

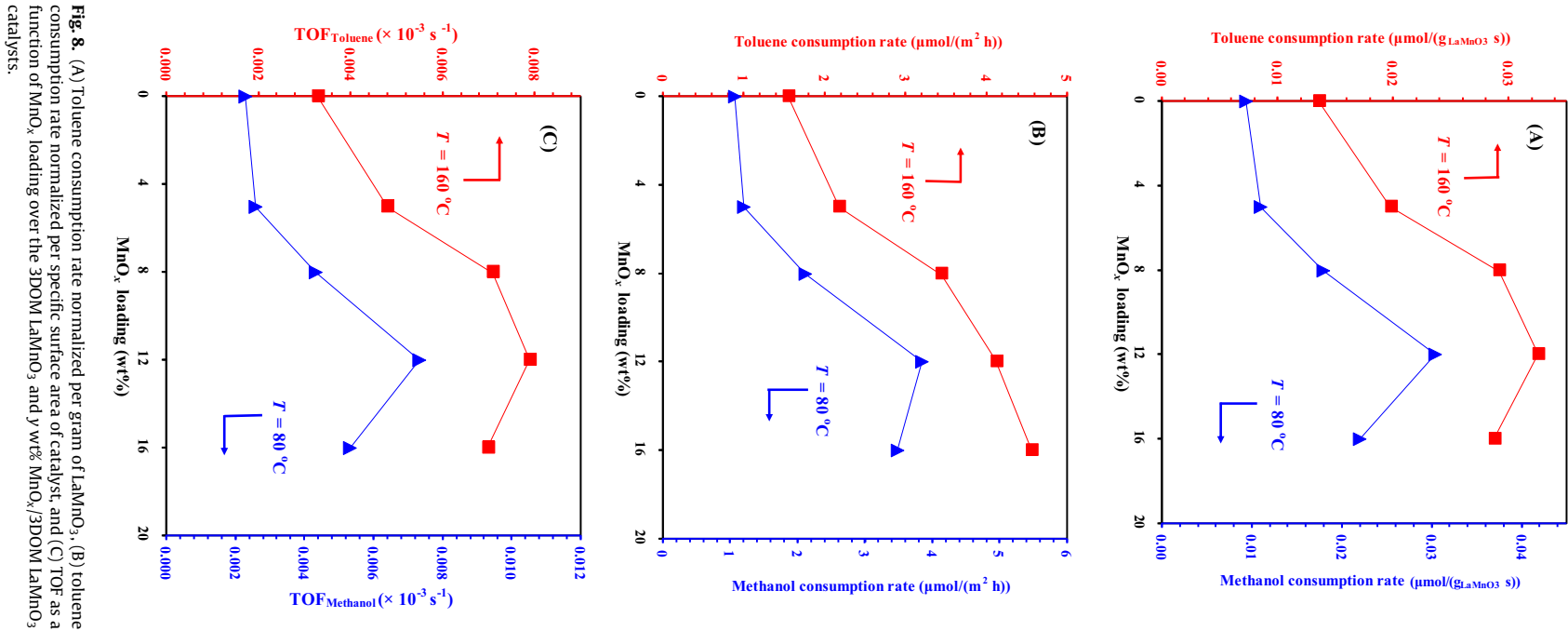
To probe the catalytic stability of the best-performing 12 wt% MnO_x/3DOM LaMnO₃ sample, we conducted the 100-h on-stream reaction experiment and the result is shown in Fig. 9. Apparently, there were no significant losses in catalytic activity within 100 h of on-stream reaction. Furthermore, the XRD pattern (Fig. S6 of the supplementary material) of the used catalyst was rather similar to that of the fresh one, and the surface area (24.5 m²/g) of the former was close to that (25.0 m²/g) of the latter. These results demonstrate that the 12 wt% MnO_x/3DOM LaMnO₃ sample was catalytically stable.

In the past years, the combustion of toluene has been studied over various catalysts, as summarized in Table 4. Among the as-prepared catalysts, the 12–16 wt% MnO_x/LaMnO₃ catalyst showed the highest toluene consumption rate per surface area (4.2–4.6 μmol/(m² h) at 160 °C), which was much higher than that (0.024 μmol/(m² h) at 160 °C) over LaMnO₃ [40], that (0.52 μmol/(m² h) at 175 °C) over La_{0.8}Sr_{0.2}MnO₃ [41], that

Table 3
The reaction rates, TOF values, and apparent activation energies for toluene and methanol combustion over the LaMnO₃ and y wt% MnO_x/LaMnO₃ samples.

Sample	Toluene combustion ^a				Methanol combustion ^a			
	Reaction rate ($\times 10^{-6}$ mol/(g s))	Reaction rate ($\times 10^{-6}$ mol/(m ² h))	TOF _{LaMnO₃} ($\times 10^{-3}$ s ⁻¹)	E _a (kJ/mol)	Reaction rate ($\times 10^{-6}$ mol/(g s))	Reaction rate ($\times 10^{-6}$ mol/(m ² h))	TOF _{LaMnO₃} ($\times 10^{-3}$ s ⁻¹)	E _a (kJ/mol)
Bulk-LaMnO ₃	0.0013	0.66	0.00032	97	0.00092	0.47	0.00022	65
3DOM LaMnO ₃	0.014	1.6	0.0033	66	0.0094	1.1	0.0023	54
5 wt% MnO _x /3DOM LaMnO ₃	0.019	2.2	0.0048	62	0.010	1.2	0.0026	54
8 wt% MnO _x /3DOM LaMnO ₃	0.027	3.5	0.0071	62	0.017	2.1	0.0043	49
12 wt% MnO _x /3DOM LaMnO ₃	0.029	4.2	0.0079	61	0.027	3.8	0.0073	48
16 wt% MnO _x /3DOM LaMnO ₃	0.025	4.6	0.0070	62	0.019	3.6	0.0053	48
12 wt% MnO _x /Bulk-LaMnO ₃	0.0018	0.86	0.00048	90	0.0012	0.60	0.00033	62

^a The reaction rates and TOF values at low conversions in a kinetically controlled regime at 160 °C for toluene combustion and at 80 °C for methanol combustion, respectively.



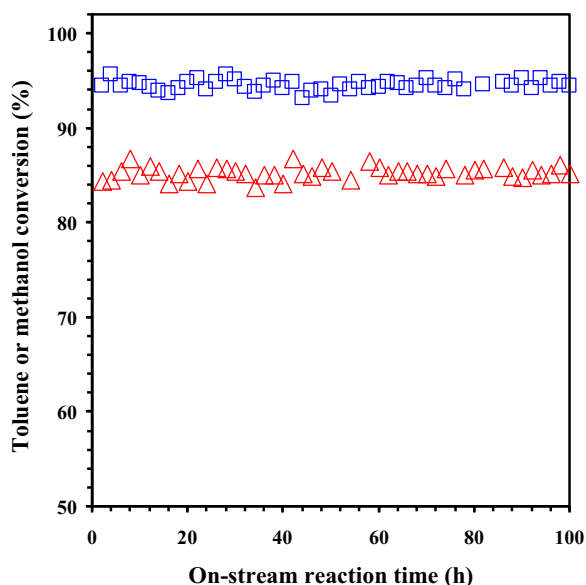


Fig. 9. Catalytic activity versus on-stream reaction time over the 12 wt% $\text{MnO}_x/3\text{DOM LaMnO}_3$ catalyst for the oxidation of (Δ) toluene at 210°C and (\square) methanol at 140°C under the conditions of VOC concentration = 1000 ppm, VOC/O_2 molar ratio = 1/400, and $\text{SV} = 20,000 \text{ mL}/(\text{g h})$.

($0.48 \mu\text{mol}/(\text{m}^2 \text{ h})$) at 160°C) over 30 wt% $\text{Co}_3\text{O}_4/\text{CeO}_2$ [42], that ($0.85 \mu\text{mol}/(\text{m}^2 \text{ h})$) at 210°C) over 4.3 wt% Au/CeO_2 [43], but much lower than that ($29.0 \mu\text{mol}/(\text{m}^2 \text{ h})$) at 160°C) over 0.5 wt% Pt/LaMnO_3 [44] and that ($9.5 \mu\text{mol}/(\text{m}^2 \text{ h})$) at 160°C) over 0.5 wt% $\text{Pd}/\text{Cr}_2\text{O}_3 - \text{ZrO}_2$ [45]. In the oxidation of methanol, the 12 wt% $\text{MnO}_x/\text{LaMnO}_3$ catalyst showed the highest rate per surface area ($3.8 \mu\text{mol}/(\text{m}^2 \text{ h})$) at 80°C), which was much higher than that ($0.012 \mu\text{mol}/(\text{m}^2 \text{ h})$) at 80°C) over 2.1 wt% $\text{Au}/\text{Fe}_2\text{O}_3$ [36], that ($0.16 \mu\text{mol}/(\text{m}^2 \text{ h})$) at 80°C) over mesoporous Fe_2O_3 [46], that ($1.37 \mu\text{mol}/(\text{m}^2 \text{ h})$) at 80°C) over mesoporous Co_3O_4 [47], and that ($1.89 \mu\text{mol}/(\text{m}^2 \text{ h})$) at 80°C) over 4.3 wt% Au/CeO_2 [43].

It has been generally accepted that performance of an ABO_3 catalyst is associated with its surface area, defect nature and density, oxygen adspecies, and reducibility. A higher surface area is beneficial for improvement in catalytic activity [48]. The presence of oxygen nonstoichiometry favors the activation of gas-phase oxygen molecules to form active oxygen adspecies. The higher the oxygen nonstoichiometry, the better is the performance of the perovskite catalyst [1,49]. The strong redox ability of ABO_3 guarantees the good recyclability of B-site ions with at least two oxidation states, and hence facilitating the combustion of organics [50]. It has been generally believed that toluene oxidation might follow a suprafacial mechanism, in which gas-phase toluene molecules first react with surface oxygen species over the $\text{La}_{1-x}\text{Sr}_x\text{MO}_{3-\delta}$ ($\text{M} = \text{Co}, \text{Mn}; x = 0, 0.4$) catalysts [51], and then the surface lattice oxygen species is involved in the oxidation of toluene; in the meanwhile, gas-phase oxygen molecules are activated to be active oxygen adspecies which can replenish the oxygen species consumed due to the reaction with toluene. With the doping of MnO_x , the $\text{Mn}^{4+}/\text{Mn}^{3+}$ and $\text{O}_{\text{ads}}/\text{O}_{\text{latt}}$ molar ratios were modified in y wt% $\text{MnO}_x/\text{LaMnO}_3$, so that an enhancement in low-temperature reducibility was achieved. This action facilitates the redox cycles in $\text{Mn}^{4+} \rightleftharpoons \text{Mn}^{3+}$ and $\text{O}_2 \rightleftharpoons \text{O}_{\text{ads}}$, thus giving rise to an improvement in catalytic activity of y wt% $\text{MnO}_x/\text{LaMnO}_3$. Compared to Bulk- LaMnO_3 (surface area = $7.3 \text{ m}^2/\text{g}$), 12 wt% $\text{MnO}_x/\text{Bulk-LaMnO}_3$ (surface area = $7.0 \text{ m}^2/\text{g}$), and 3DOM LaMnO_3 (surface area = $31.4 \text{ m}^2/\text{g}$), the y wt% $\text{MnO}_x/3\text{DOM LaMnO}_3$ samples (surface area = $19.1\text{--}31.0 \text{ m}^2/\text{g}$) exhibited much higher VOC consumption

rates (Figs. 7–10). This result suggest that the higher surface oxygen species concentration and better low-temperature reducibility induced by the $\text{MnO}_x\text{--LaMnO}_3$ interaction might play an important role in catalyzing the combustion of toluene and methanol. As shown in Fig. S7 of the supplementary material, the toluene or methanol reaction rate at each temperature increased with the rise in $\text{O}_{\text{ads}}/\text{O}_{\text{latt}}$ molar ratio. That is to say, a higher O_{ads} concentration was beneficial for the enhancement in catalytic performance of the y wt% $\text{MnO}_x/3\text{DOM LaMnO}_3$ samples. From Figs. 5 and 6 and Table 2, one can see that the best-performing 12 wt% $\text{MnO}_x/\text{LaMnO}_3$ catalyst possessed the highest oxygen adspecies concentration and the best low-temperature reducibility. In addition, a strong interaction between MnO_x and 3DOM LaMnO_3 was also one of the factors that led to enhanced catalytic activities of y wt% $\text{MnO}_x/\text{LaMnO}_3$. The formed nanostructural heterojunctions on the $\text{MnO}_x/\text{LaMnO}_3$ composite surface would give rise to a more efficient electron transfer between the two components [52,53]. Due to strong interaction between MnO_x and LaMnO_3 catalytic activity of supported catalysts depended not only on the single phases of MnO_x and LaMnO_3 but also was determined by character of the $\text{MnO}_x\text{--LaMnO}_3$ interaction. Therefore, we conclude that the excellent catalytic performance of 12 wt% $\text{MnO}_x/\text{LaMnO}_3$ was related to the highest oxygen adspecies concentration and best low-temperature reducibility as well as the synergistic interaction between MnO_x and 3DOM LaMnO_3 .

3.6. Apparent activation energy

The kinetics of catalytic oxidation of VOCs has been gained much attention. There are several reports related to the catalytic kinetic behaviors of VOC combustion in the literature. For instance, good linear Arrhenius plots were obtained over the ceria-zirconia-supported LaCoO_3 catalysts when toluene oxidation was first-order and zero-order kinetics with respect to toluene and oxygen [54], respectively. Hence, it can be reasonably assumed that in the presence of excess oxygen, toluene and methanol oxidation would obey a first-order reaction mechanism with respect to VOC concentration (c , $\mu\text{mol}/\text{g}$): $r = -kc = (-A \exp(-E_a/RT)) c$, where r , k , A , and E_a are the reaction rate ($\mu\text{mol}/(\text{g s})$), rate constant (s^{-1}), pre-exponential factor, and apparent activation energy (kJ/mol), respectively.

Fig. 10 shows the Arrhenius plots for the combustion of toluene and methanol over the LaMnO_3 and y wt% $\text{MnO}_x/\text{LaMnO}_3$ catalysts at a VOC conversion of $< 20\%$, respectively. Excellent linear relationships (the correlation coefficients (R^2) were rather close to 1) of $\ln k$ versus $1000/T$ for all of the catalysts were obtained. The E_a value ($97 \text{ kJ}/\text{mol}$ for toluene combustion and $65 \text{ kJ}/\text{mol}$ for methanol combustion) of the Bulk- LaMnO_3 catalyst was much higher than those ($61\text{--}66 \text{ kJ}/\text{mol}$ for toluene combustion and $48\text{--}54 \text{ kJ}/\text{mol}$ for methanol combustion) of the 3DOM LaMnO_3 and y wt% $\text{MnO}_x/3\text{DOM LaMnO}_3$ catalysts. By comparing the E_a values of different catalysts, one can evaluate their catalytic performance. The lower the E_a value, the easier the complete oxidation of organics, and hence the better is the performance of a catalyst. The discrepancy in E_a value might be due to the differences in pore structure, oxygen nonstoichiometry, and low-temperature reducibility of the as-prepared catalysts. In the case of toluene combustion, the apparent activation energies ($61\text{--}62 \text{ kJ}/\text{mol}$) of y wt% $\text{MnO}_x/3\text{DOM LaMnO}_3$ were close to those ($51\text{--}79 \text{ kJ}/\text{mol}$) of $\text{LaCoO}_3/\text{Ce}_{1-x}\text{Zr}_x\text{O}_2$ ($x = 0\text{--}0.2$) [54] and that ($62 \text{ kJ}/\text{mol}$) of $\text{Pt}/\text{Ce}_{0.64}\text{Zr}_{0.15}\text{Bi}_{0.21}\text{O}_{1.895}/\text{Al}_2\text{O}_3$ [55], but much lower than those ($120\text{--}144 \text{ kJ}/\text{mol}$) of $\text{CuO}/\text{Al}_2\text{O}_3$ and $\text{MnO}/\text{Al}_2\text{O}_3$ [56]. In the case of methanol combustion, the apparent activation energies ($48\text{--}54 \text{ kJ}/\text{mol}$) of y wt% $\text{MnO}_x/3\text{DOM LaMnO}_3$ were similar to that ($50 \text{ kJ}/\text{mol}$) of mesoporous Co_3O_4 [47], but slightly lower than that ($61 \text{ kJ}/\text{mol}$) of mesoporous

Table 4

The reaction rates of various catalysts for VOC combustion reported in the literature.

Catalyst	Reaction temperature (°C)	Reaction rate ($\times 10^{-6}$ mol/(g s))	Reaction rate ($\times 10^{-6}$ mol/(m ² h))	Ref.
16 wt% MnO _x /3DOM LaMnO ₃	160	0.025	4.6	This work
LaMnO ₃	160	0.000098	0.024	[32]
La _{0.8} Sr _{0.2} MnO ₃	175	0.0032	0.52	[33]
20 wt% LaCoO ₃ /Ce _{0.9} Zr _{0.1} O ₂	160	0.082	14.5	[46]
30 wt% Co ₃ O ₄ –CeO ₂	160	0.0044	0.48	[34]
4.3 wt% Au/CeO ₂	210	0.028	0.85	[35]
0.5 wt% Pt/LaMnO ₃	160	0.14	29.0	[36]
0.5 wt% Pd/Cr ₂ O ₃ –ZrO ₂	160	0.079	9.5	[37]
12 wt% MnO _x /3DOM LaMnO ₃	80	0.027	3.8	This work
Fe ₂ O ₃	80	0.0058	0.16	[38]
Co ₃ O ₄	80	0.046	1.37	[39]
2.1 wt% Au/Fe ₂ O ₃	80	0.00067	0.012	[29]
4.3 wt% Au/CeO ₂	80	0.062	1.89	[35]

Fe₂O₃ [46] and that (61 kJ/mol) of Pt/ γ -Al₂O₃ [57]. Therefore, the results of kinetic investigations confirm that the 3DOM-structured MnO_x/LaMnO₃ catalysts showed excellent catalytic performance for the combustion of toluene and methanol at low temperatures.

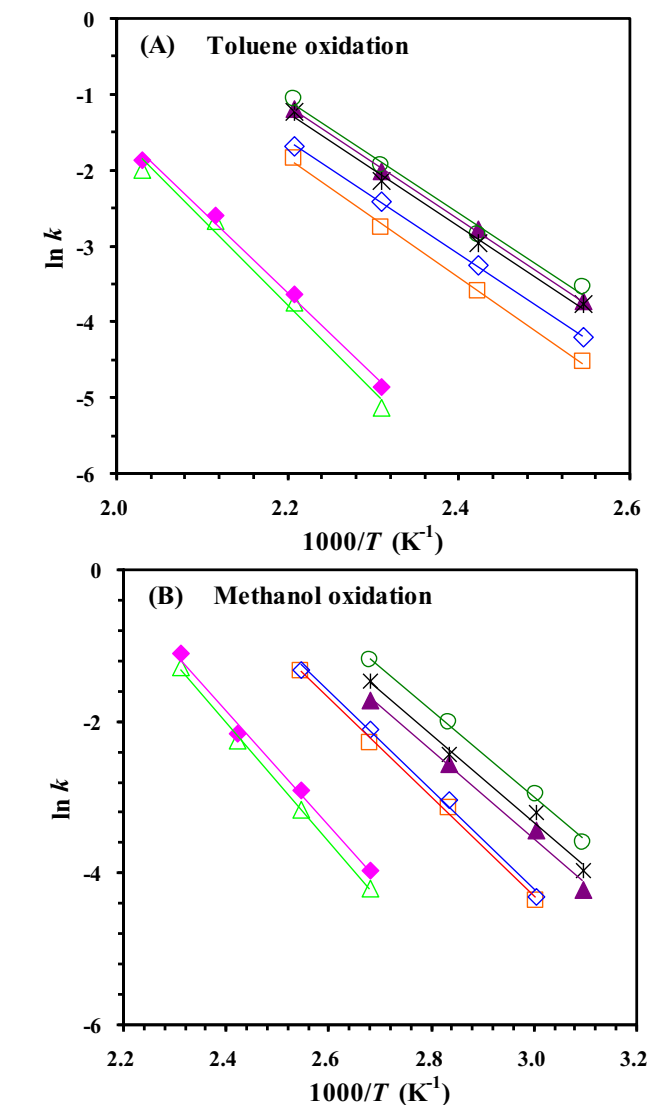


Fig. 10. Arrhenius plots for the oxidation of (A) toluene and (B) methanol over (□) 3DOM LaMnO₃, (◇) 5 wt% MnO_x/3DOM LaMnO₃, (▲) 8 wt% MnO_x/3DOM LaMnO₃, (○) 12 wt% MnO_x/3DOM LaMnO₃, (✱) 16 wt% MnO_x/3DOM LaMnO₃, (△) Bulk-LaMnO₃, (◆) 12 wt% MnO_x/Bulk-LaMnO₃.

4. Conclusions

3DOM-structured LaMnO₃ and its supported MnO_x (y wt% MnO_x/3DOM LaMnO₃, $y=0, 5, 8, 12$, and 16) catalysts were prepared via an in situ tryptophan-assisted PMMA-templating route. The y wt% MnO_x/3DOM LaMnO₃ samples displayed a 3DOM architecture with a rhombohedral perovskite crystal structure and a surface area of 19–31 m²/g, among which the 12 wt% MnO_x/3DOM LaMnO₃ sample contained small MnO_x particles (size = 4–18 nm) highly dispersed on the surface of 3DOM LaMnO₃. XPS results reveal that the 12 wt% MnO_x/3DOM LaMnO₃ sample possessed the highest oxygen adspecies concentration. H₂-TPR results demonstrate that the y wt% MnO_x/3DOM LaMnO₃ samples exhibited better low-temperature reducibility than the bulk and MnO_x-free counterparts, with the 12 wt% MnO_x/3DOM LaMnO₃ sample showing the best low-temperature reducibility. Under the conditions of toluene or methanol concentration = 1000 ppm, toluene or methanol/O₂ molar ratio = 1/400, SV = 20,000 mL/(g h), and VOC conversion < 15%, the 12 wt% MnO_x/3DOM LaMnO₃ sample giving the highest TOF values of $7.9 \times 10^{-6} \text{ s}^{-1}$ for toluene combustion at 160 °C and $7.3 \times 10^{-6} \text{ s}^{-1}$ for methanol combustion at 80 °C. The apparent activation energies of the y wt% MnO_x/3DOM LaMnO₃ catalysts were 61–62 and 48–54 kJ/mol for toluene and methanol combustion, respectively. Based on the activity data and characterization results, we conclude that high oxygen adspecies concentration, good low-temperature reducibility, and strong interaction between MnO_x and 3DOM LaMnO₃ were responsible for the excellent catalytic performance of 12 wt% MnO_x/3DOM LaMnO₃ for toluene and methanol combustion.

Acknowledgements

The work described was supported by the NSF of China (20973017 and 21077007), the Discipline and Postgraduate Education (005000541212014), the NSF of Beijing Municipality (2102008), the Creative Research Foundation of Beijing University of Technology (00500054R4003 and 005000543111501), and the Funding Project for Academic Human Resources Development in Institutions of Higher Learning under the Jurisdiction of Beijing Municipality (PHR201207105 and PHR201207104). We also thank Prof. Chak Tong Au (Department of Chemistry, Hong Kong Baptist University) and Mrs. Jianping He (State Key Laboratory of Advanced Metals and Materials, University of Science & Technology Beijing) for doing the XPS and SEM analyses of the samples, respectively.

Appendix A. Supplementary data

Supplementary data associated with this article can be found, in the online version, at <http://dx.doi.org/10.1016/j.apcatb.2013.04.051>.

References

- [1] M.A. Peña, J.L.G. Fierro, *Chemical Reviews* 101 (2001) 1981–2018.
- [2] H. Fujii, N. Mizuno, M. Misono, *Chemistry Letters* 11 (1987) 2147–2150.
- [3] S. Colonna, S. De Rossi, M. Faticanti, I. Pettiti, P. Porta, *Journal of Molecular Catalysis A* 187 (2002) 269–276.
- [4] M. Alifanti, M. Florea, V.I. Pârvulescu, *Applied Catalysis B* 70 (2007) 400–405.
- [5] A. Galenda, M.M. Natile, A. Glisenti, *Journal of Molecular Catalysis A* 282 (2008) 52–61.
- [6] L. Wang, S.-Q. Chen, Y. Liu, *Acta Physico-Chimica Sinica* 24 (2008) 849–854.
- [7] Y.Z. Fang, Y. Liu, L.H. Zhang, *Applied Catalysis A* 397 (2011) 183–191.
- [8] S.J. Tauster, S.C. Fung, R.L. Garten, *Journal of the American Chemical Society* 100 (1978) 170–175.
- [9] F. Wyrwalski, J.-F. Lamonier, S. Siffert, A. Aboukaïs, *Applied Catalysis B* 70 (2007) 393–399.
- [10] Z.K. Zhao, X.L. Lin, R.H. Jin, G.R. Wang, T. Muhammad, *Applied Catalysis B* 115–116 (2012) 53–62.
- [11] A.P. Jia, G.S. Hu, L. Meng, Y.L. Xie, J.Q. Lu, M.F. Luo, *Journal of Catalysis* 289 (2012) 199–209.
- [12] M. Sadakane, T. Horiuchi, N. Kato, C. Takahashi, W. Ueda, *Chemistry of Materials* 19 (2007) 5779–5785.
- [13] H.N. Li, L. Zhang, H.X. Dai, H. He, *Inorganic Chemistry* 48 (2009) 4421–4434.
- [14] P. Ciambelli, S. Cimino, S.-D. Rossi, M. Faticanti, L. Lisi, G. Minelli, I. Pettiti, P. Porta, G. Russo, M. Turco, *Applied Catalysis B* 24 (2000) 243–253.
- [15] E.R. Stobbe, B.A. de Boer, J.W. Geus, *Catalysis Today* 47 (1999) 161–167.
- [16] P. Esmaeilnejad-Ahranjani, A. Khodadadi, H. Ziaei-Azad, Y. Mortazavi, *Chemical Engineering Journal* 169 (2011) 282–289.
- [17] Z.B. He, S.H. Yu, J.P. Zhu, *Chemistry of Materials* 17 (2005) 2785–2788.
- [18] Z.Y. Zhong, J.Y. Lin, S.P. Teh, J. Teo, F.M. Dautzenberg, *Advanced Functional Materials* 17 (2007) 1402–1408.
- [19] W. Buchmann, R. Spezia, G. Tournois, T. Cartailier, J. Tortajada, *Journal of Mass Spectrometry* 42 (2007) 517–526.
- [20] S. Ponce, M.A. Peña, J.L.G. Fierro, *Applied Catalysis B* 24 (2000) 193–205.
- [21] J.-M. Giraudon, A. Elhachimi, G. Leclercq, *Applied Catalysis B* 84 (2008) 251–261.
- [22] Y.N. Lee, R.M. Lago, J.L.G. Fierro, V. Cortés, F. Sapiña, E. Martínez, *Applied Catalysis A* 207 (2001) 17–24.
- [23] Y.X. Liu, H.X. Dai, Y.C. Du, J.G. Deng, L. Zhang, Z.X. Zhao, *Applied Catalysis B* 119–120 (2012) 20–31.
- [24] S. Rousseau, S. Loricant, P. Delichere, A. Boreave, J.P. Deloume, P. Vernoux, *Applied Catalysis B* 88 (2009) 438–447.
- [25] H.T. Tan, Y.T. Chen, C.M. Zhou, X.L. Jia, J.X. Zhu, J. Chen, X.H. Rui, Q.Y. Yan, Y.H. Yang, *Applied Catalysis B* 119–120 (2012) 166–174.
- [26] M.L. Cubeiro, J.L.G. Fierro, *Journal of Catalysis* 179 (1998) 150–162.
- [27] H. Najjar, H. Batis, *Applied Catalysis A* 383 (2010) 192–201.
- [28] R. Hammami, S.B. Aïssa, H. Batis, *Applied Catalysis A* 353 (2009) 145–153.
- [29] Z.P. Qu, Y.B. Bu, Y. Qin, Y. Wang, Q. Fu, *Applied Catalysis B* 132–133 (2013) 353–362.
- [30] S. Kumar, Y. Teraoka, A.G. Joshi, S. Rayalu, N. Labhsetwar, *Journal of Molecular Catalysis A* 348 (2011) 42–54.
- [31] F. Teng, W. Han, S.H. Liang, B. Gaugeu, R.L. Zong, Y.F. Zhu, *Journal of Catalysis* 250 (2007) 1–11.
- [32] H.J. Wei, Y. Cao, W.J. Ji, C.T. Au, *Catalysis Communications* 9 (2008) 2509–2514.
- [33] Z. Sarshar, F. Kleitz, S. Kaliaguine, *Energy & Environmental Science* 4 (2011) 4258–4269.
- [34] J. Töpfer, J.B. Goodenough, *Journal of Solid State Chemistry* 130 (1997) 117–128.
- [35] J. Töpfer, J.B. Goodenough, *Chemistry of Materials* 9 (1997) 1467–1474.
- [36] S. Minico, S. Scire, C. Crisafulli, R. Maggiore, S. Galvango, *Applied Catalysis B* 28 (2000) 245–251.
- [37] K.D. Chen, S.B. Xie, A.T. Bell, E. Iglesia, *Journal of Catalysis* 198 (2001) 232–242.
- [38] P.B. Weisz, C.D. Prater, *Advances in Catalysis* 6 (1954) 143–196.
- [39] J. Xu, L. Ouyang, W. Mao, X.J. Yang, X.C. Xu, J.J. Su, T.Z. Zhuang, H. Li, Y.F. Han, *ACS Catalysis* 2 (2012) 261–269.
- [40] S. Iruata, M.P. Pina, M. Menéndez, J. Santamaría, *Journal of Catalysis* 179 (1998) 400–412.
- [41] V. Blasin-Aubé, J. Belkouch, L. Monceaux, *Applied Catalysis B* 43 (2003) 175–186.
- [42] L.F. Liotta, M. Ousmane, G. Di Carlo, G. Pantaleo, G. Deganello, A. Boreave, A. Giroir-Fendler, *Catalysis Letters* 127 (2009) 270–276.
- [43] S. Scire, P.M. Riccobene, C. Crisafulli, *Applied Catalysis B* 101 (2010) 109–117.
- [44] A. Musialik-Piotrowska, H. Landmesser, *Catalysis Today* 137 (2008) 357–361.
- [45] L.Y. Jin, R.H. Ma, J.J. Lin, L. Meng, Y.J. Wang, M.F. Luo, *Industrial and Engineering Chemistry Research* 50 (2011) 10878–10882.
- [46] Y.S. Xia, H.X. Dai, H.Y. Jiang, L. Zhang, J.G. Deng, Y.X. Liu, *Journal of Hazardous Materials* 186 (2011) 84–91.
- [47] Y.S. Xia, H.X. Dai, H.Y. Jiang, L. Zhang, *Catalysis Communications* 11 (2010) 1171–1175.
- [48] N. Gunasekaran, S. Saddawi, J.J. Carberry, *Journal of Catalysis* 159 (1996) 107–111.
- [49] J.G. Deng, L. Zhang, H.X. Dai, H. He, C.T. Au, *Applied Catalysis B* 89 (2009) 87–96.
- [50] T. Nakamura, M. Misono, Y. Yoneda, *Chemistry Letters* 10 (1981) 1589–1592.
- [51] J.G. Deng, L. Zhang, H.X. Dai, H. He, C.T. Au, *Industrial and Engineering Chemistry Research* 47 (2008) 8175–8183.
- [52] H.J. Huang, D.Z. Li, Q. Lin, W.J. Zhang, Y. Shao, Y.B. Chen, M. Sun, X.Z. Fu, *Environmental Science and Technology* 43 (2009) 4164–4168.
- [53] J. Lv, T. Kako, Z.S. Li, Z.G. Zou, J.H. Ye, *Journal of Physical Chemistry C* 114 (2010) 6157–6162.
- [54] M. Alifanti, M. Florea, S. Somacescu, V.I. Pârvulescu, *Applied Catalysis B* 60 (2005) 33–39.
- [55] T. Masui, H. Imadzu, N. Matsuyama, N. Imanaka, *Journal of Hazardous Materials* 176 (2010) 1106–1109.
- [56] S.M. Saqer, D.I. Kondarides, X.E. Verykios, *Applied Catalysis B* 103 (2011) 275–286.
- [57] J. Pasel, B. Emonts, R. Peters, D. Stolten, *Catalysis Today* 69 (2001) 193–200.